Direct Power Control of Doubly Fed Induction Generator Without Phase-Locked Loop Under Harmonically Distorted Voltage Conditions

Heng Nian, *Senior Member, IEEE*, and Longqi Li

***Abstract*—This paper proposes an improved direct power control (DPC) strategy of the doubly fed induction generator without phase-locked loop (PLL) under harmonically distorted voltage conditions. The proposed DPC scheme is implemented in a virtual synchronous reference frame, so that the potential instability problems caused by PLL can be eliminated. A second-order vector integrator is integrated with DPC to suppress the harmonic components directly, so that three different control targets of smooth stator active and reactive powers, sinusoidal stator current and constant electromagnetic torque, can be achieved. The sequential separations and the complex calculations of the power compensating items can also be eliminated. Meanwhile, a simple grid frequency estimation scheme is proposed, which can make the control strategy self-adaptive to the frequency variation in the practical situation. Finally, the experimental results validate the availability of the proposed DPC strategy.**

***Index Terms*—Direct power control (DPC), distorted voltage, doubly fed induction generator (DFIG), frequency adaptive, frequency deviation, no phase-locked loop (PLL), second-order vector integrator (SOVI).**

I. Introduction

WIND power generation systems based on the doubly fed induction generators (DFIGs) have been widely employed due to the variable-speed constant-frequency operation, four quarter active and reactive power regulation and smaller converter rating, compared to the fixed speed induction generators and the permanent magnet synchronous generators [1], [2]. Several control strategies have been proposed to improve the DFIG operation performance, which can be mainly divided into the vector control (VC) and direct power control (DPC). Compared with VC schemes, DPC strategy can avoid the complex configuration of the commanded current calculation and achieve the direct power regulation and fast dynamic response, with less dependence on generator parameters [3].

However, since DFIG-based wind energy conversion systems are usually equipped in the rural grid and distribution network with long transmission lines, the harmonic distortions (typical the fifth and seventh order) have become a common adverse disturbance in the grid voltage [4]. Thus, without the harmonic distortions taken into account, the DFIG system operation performance will be jeopardized, which will cause the highly distorted stator current, significant electromagnetic torque, and power oscillations.

Therefore, in order to improve the operation performance of DFIG system under distorted grid conditions, several associated control schemes based on DPC have been proposed. In [5] and [6], a proportional integral plus resonant controller was implemented to eliminate the distorted stator current, or suppress power pulsations, or smooth electromagnetic torque ripples in the synchronous reference frame. However, the extractions of the fifth- and seventh-order harmonic of the voltages and currents and complex calculations of the control references are involved, which deteriorates the dynamic response and control accuracy of the DFIG system. In order to avoid complex calculations and sequence decompositions, in [7] and [8], an auxiliary resonant closed-loop control was added in the power regulation loop, which can successfully eliminate the harmonic components of active and reactive powers. However, the control target of sinusoidal output current was ignored.

Nevertheless, the control strategies mentioned above are implemented in the synchronous reference frame in conjunction with the phase-locked loop (PLL), whose behavior will worsen with the phase detection error under the distorted voltage. In order to accurately track the voltage vector position, some modified PLLs were presented, such as multiple second-order generalized integrator based PLL [9], multiple complex coefficient filter based PLL [10], etc. Furthermore, the small signal analysis of three-phase inverter on PLL was given in [11]–[13], which pointed out that the negative incremental resistor caused by PLL would lead the system into the unstable situation. Thus, it is attractive to develop a control strategy without PLL for DFIG system under distorted voltage conditions.

In order to avoid the potential instability problems caused by PLL, in [14] and [15], the DPC scheme was implemented in a synchronous reference frame with a virtual phase angle in-

Manuscript received January 17, 2017; revised May 8, 2017; accepted August 11, 2017. Date of publication August 14, 2017; date of current version March 5, 2018. This work was supported in part by the National Natural Science Foundation of China under Grant 51622706, and the Fundamental Research Funds for the Central Universities under Grant 2017XZZX002-17. Recommended for publication by Associate Editor P. C.-K. Luk. *(Corresponding author: Heng Nian.)*

The authors are with the College of Electrical Engineering, Zhejiang University, Hangzhou 310027, China (e-mail: nianheng@zju.edu.cn; lilongqi321@163.com).

Color versions of one or more of the figures in this paper are available online at http://ieeexplore.ieee.org.

Digital Object Identifier 10.1109/TPEL.2017.2740265

stead of the voltage phase angle acquired by the PLL during network unbalances. However, when the DFIG system operates under distorted grid conditions, the performance of resonant regulators employed in [14] and [15] will deteriorate in the presence of frequency variation. It is noted that potential frequency variation usually occurs in the grid network, according to grid codes, such as ± 1 Hz [16] and -3 Hz/$+2$ Hz [17]. During the transient frequency variation, the power and torque pulsations of fundamental frequency caused by natural flux linkages will occur, and a demagnetizing current control scheme was proposed in [18]. Furthermore, as the grid frequency deviates from nominal one, the deviation range of the harmonic frequency will become even larger. Since resonant regulators can only provide infinite gain in the specific frequency, the ability to suppress harmonic components will be seriously degraded when the practical frequency encounters disturbances. Therefore, it is quite essential to develop a frequency adaptive control strategy without PLL for the DFIG system.

This paper investigates the DPC strategy without PLL involved for DFIG system under distorted grid voltage conditions. A second-order vector integrator (SOVI) is employed to eliminate the harmonic components of currents, powers or electromagnetic torque directly, and three different control targets of smooth active and reactive power, sinusoidal stator current or smooth electromagnetic torque can be achieved. Meanwhile, a frequency estimation algorithm is proposed to make the SOVI frequency adaptive, which guarantees the accurate harmonic suppression capability in the presence of frequency variation.

This paper will be organized as follows. Section II analyzes the mathematical model of a DFIG system in an arbitrary synchronous reference frame without PLL under distorted voltage conditions. Then, a control scheme with an SOVI controller employed is put forward to improve system operation performance in Section III. Then, a frequency estimation algorithm is proposed in Section IV. The performance of the proposed DPC control strategy is analyzed theoretically in Section V. Experimental validations are conducted in Section VI. Finally, the conclusions are made in Section VII.

II. Mathematical Model of the DFIG System Without PLL

In order to investigate the DPC scheme of the DFIG system, the mathematical models under distorted voltage conditions should be built first. The models are established in an arbitrary synchronous reference frame rotating at the fixed angular speed $\omega_1 = 100\pi$ rad/s, and a virtual phase angle $\theta_1 = \omega_1 t$ is employed to replace the actual one acquired by the PLL for the coordinate transformations. Different from the models in [15], the harmonic voltage components will be considered in the models and the relevant control strategies will be deduced. It should be noted that only fifth- and seventh-harmonic frequency components are considered in this paper, the research can also be applied for the grid voltage with the higher harmonics.

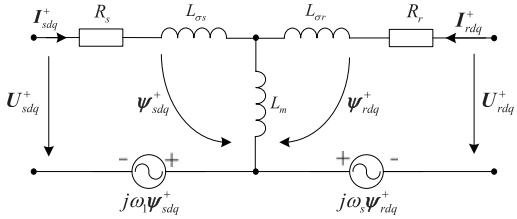

Fig. 1. Equivalent circuit of a DFIG in the $(dq)^+$ reference frame.

Under distorted voltage conditions, the voltages, currents, and flux linkages contain the fundamental frequency components and fifth- and seventh-harmonic frequency components. Here, a variable $\boldsymbol{F}$ is defined to represent the vectors above, and can be expressed in the stationary $(\alpha\beta)$ reference frame as

$$\begin{aligned}\boldsymbol{F}_{\alpha\beta} &= \boldsymbol{F}_{\alpha\beta+} + \boldsymbol{F}_{\alpha\beta 5-} + \boldsymbol{F}_{\alpha\beta 7+} \\ &= F_+ e^{j\omega_g t} + F_{5-} e^{-j5\omega_g t} + F_{7+} e^{j7\omega_g t}\end{aligned} \tag{1}$$

where the subscripts $+$, $5-$, and $7+$ represent the fundamental components and fifth- and seventh-harmonic components, respectively, ω_g is the actual angular speed of $\boldsymbol{F}$, F_+, F_{5-}, and F_{7+} are the amplitudes of the fundamental components and fifth- and seventh-harmonic components, respectively.

Then, with the virtual phase angle θ, $\boldsymbol{F}$ can be transformed into the virtual synchronous reference frame.

$$\begin{aligned}\boldsymbol{F}^+_{dq} &= \boldsymbol{F}_{\alpha\beta} \cdot e^{-j\omega_1 t} = \boldsymbol{F}^+_{dq+} + \boldsymbol{F}^+_{dq5-} + \boldsymbol{F}^+_{dq7+} \\ &= F_+ e^{j(\omega_g - \omega_1)t} + F_{5-} e^{-j(5\omega_g + \omega_1)t} + F_{7+} e^{j(7\omega_g - \omega_1)t}\end{aligned} \tag{2}$$

where superscript $+$ refers to the virtual synchronous $(dq)^+$ reference frame rotating at ω_1.

According to (2), if the actual angular speed ω_g is equal to the fixed one ω_1, the fundamental components behave as dc signals, and the harmonic components behave as six times the grid frequency signals. Otherwise, the fundamental components behave as low-frequency ac signals of $|\omega_g - \omega_1|$ and the harmonic components behave as ac signals of $|5\omega_g + \omega_1|$ and $|7\omega_g - \omega_1|$ if ω_g differs from ω_1.

The equivalent circuit of a DFIG in the $(dq)^+$ reference frame is shown in Fig. 1, and accordingly, the stator and rotor voltages and flux linkages can be expressed as

$$\begin{cases}\boldsymbol{U}^+_{sdq} = R_s \boldsymbol{I}^+_{sdq} + d\boldsymbol{\psi}^+_{sdq}/dt + j\omega_1 \boldsymbol{\psi}^+_{sdq} \\ \boldsymbol{U}^+_{rdq} = R_r \boldsymbol{I}^+_{rdq} + d\boldsymbol{\psi}^+_{rdq}/dt + j\omega_s \boldsymbol{\psi}^+_{rdq}\end{cases} \tag{3}$$

$$\begin{cases}\boldsymbol{\psi}^+_{sdq} = L_s \boldsymbol{I}^+_{sdq} + L_m \boldsymbol{I}^+_{rdq} \\ \boldsymbol{\psi}^+_{rdq} = L_m \boldsymbol{I}^+_{sdq} + L_r \boldsymbol{I}^+_{rdq}\end{cases} \tag{4}$$

where $\boldsymbol{U}$ is the voltage, ψ is the flux linkage, $\boldsymbol{I}$ is the current, ω_r is the rotor angular speed, $\omega_s = \omega_1 - \omega_r$ is the slip angular speed, R_s and R_r are stator and rotor resistances, $L_{\sigma s}$, $L_{\sigma r}$, and L_m are stator and rotor leakage inductances and mutual inductance, $L_s = L_m + L_{\sigma s}$ and $L_r = L_m + L_{\sigma r}$ are the self-inductances of stator and rotor windings, respectively.

The stator active and reactive powers can be calculated by

$$\boldsymbol{S}_s = P_s - jQ_s = 1.5\hat{\boldsymbol{U}}^+_{sdq} \cdot \boldsymbol{I}^+_{sdq} \tag{5}$$

where superscript ˆ refers to the conjugate complex.

The electromagnetic torque can be calculated as

$$T_e = -1.5 n_p \mathrm{Im}\left\{\boldsymbol{\psi}^+_{sdq}\hat{\boldsymbol{I}}^+_{sdq}\right\} \tag{6}$$

where n_p represent the number of the pole pairs.

Substituting (2) into (5) and (6), the stator active and reactive powers and the electromagnetic torque can be decomposed into components with different frequencies as

$$\begin{aligned} P_s &= P_{s0} + P_{s\sin 6}\sin(6\omega_g t) + P_{s\cos 6}\cos(6\omega_g t) \\ &\quad + P_{s\sin 12}\sin(12\omega_g t) + P_{s\cos 12}\cos(12\omega_g t) \end{aligned} \tag{7}$$

$$\begin{aligned} Q_s &= Q_{s0} + Q_{s\sin 6}\sin(6\omega_g t) + Q_{s\cos 6}\cos(6\omega_g t) \\ &\quad + Q_{s\sin 12}\sin(12\omega_g t) + Q_{s\cos 12}\cos(12\omega_g t) \end{aligned} \tag{8}$$

$$\begin{aligned} T_e &= T_{e0} + T_{esin6}\sin(6\omega_g t) + T_{ecos6}\cos(6\omega_g t) \\ &\quad + T_{esin12}\sin(12\omega_g t) + T_{ecos12}\cos(12\omega_g t) \end{aligned} \tag{9}$$

where subscripts 0, sin6/cos6 and sin12/cos12 represent the dc component and the cosine/sine components with the frequencies of $6\omega_g$ and $12\omega_g$.

According to (7)–(9), it can be concluded that, both the stator active/reactive powers and the torque contain oscillations at the frequencies of $6\omega_g$ and $12\omega_g$. Since the oscillating components of $12\omega_g$ are produced by the interactions between fifth- and seventh-harmonic components, which are much less significant and can be ignored in the system control.

According to (4), the rotor flux linkage can be rewritten as

$$\boldsymbol{\psi}^+_{rdq} = \frac{L_r}{L_m}\boldsymbol{\psi}^+_{sdq} - \frac{\sigma L_r L_s}{L_m}\boldsymbol{I}^+_{sdq} \tag{10}$$

where $\sigma = 1 - L_m^2/(L_s L_r)$.

Based on (3) and (10), the rotor voltage can be calculated by

$$\begin{aligned} \boldsymbol{U}^+_{rdq} &= R_r\boldsymbol{I}^+_{rdq} + \frac{L_r}{L_m}\frac{d\boldsymbol{\psi}^+_{sdq}}{dt} - \frac{\sigma L_r L_s}{L_m}\frac{d\boldsymbol{I}^+_{sdq}}{dt} \\ &\quad + j(\omega_1 - \omega_r)\left(\frac{L_r}{L_m}\boldsymbol{\psi}^+_{sdq} - \frac{\sigma L_r L_s}{L_m}\boldsymbol{I}^+_{sdq}\right). \end{aligned} \tag{11}$$

According to (5), the stator current can be expressed as

$$\boldsymbol{I}^+_{sdq} = \frac{\boldsymbol{S}_s}{1.5\hat{\boldsymbol{U}}^+_{sdq}} = \frac{2\boldsymbol{U}^+_{sdq}}{3U_s^2}\boldsymbol{S}_s \tag{12}$$

where U_s is the amplitude of the stator voltage.

Then, the differential of the stator current can be calculated as

$$\begin{aligned} \frac{d}{dt}\boldsymbol{I}^+_{sdq} &= \frac{d}{dt}\left\{\frac{2\boldsymbol{U}^+_{sdq}}{3U_s^2}\boldsymbol{S}_s\right\} = \frac{2\boldsymbol{U}^+_{sdq}}{3U_s^2}\cdot\frac{d}{dt}\boldsymbol{S}_s \\ &\quad + \boldsymbol{S}_s\cdot\frac{d}{dt}\left(\frac{2\boldsymbol{U}^+_{sdq}}{3U_s^2}\right). \end{aligned} \tag{13}$$

It should be noted that there are harmonic ripples in the stator voltage amplitude U_s under distorted voltage conditions. According to the grid standard [19], the proportion of harmonic voltage components is normally 3%–5%, which is a relatively smaller proportion compared with the fundamental ones. Thus, U_s can be appropriately regarded as constant for simplified analysis. Therefore, according to (2), the differential of the stator voltage in (13) is expressed as

$$\begin{aligned} &\frac{d}{dt}\left(\frac{2\boldsymbol{U}^+_{sdq}}{3U_s^2}\right) = \\ &\frac{2}{3U_s^2}\begin{bmatrix} j(\omega_g - \omega_1)\boldsymbol{U}^+_{sdq+} - j(5\omega_g + \omega_1)\boldsymbol{U}^+_{sdq5-} \\ +j(7\omega_g - \omega_1)\boldsymbol{U}^+_{sdq7+} \end{bmatrix}. \end{aligned} \tag{14}$$

In consideration of the fact that the actual angular is at the adjacent of the nominal one, the mismatch can be ignored for simplified analysis. Thus, the first term in (14) can be neglected. Besides, the ratio of the harmonic voltage components is relatively smaller, so the other two items in (14) are supposed to be null. In this way, according to (3) and (13), (11) can be rewritten as

$$\begin{aligned} \boldsymbol{U}^+_{rdq} &= \frac{L_r}{L_m}\left\{\boldsymbol{U}^+_{sdq} + \left(\frac{R_r}{L_r} - j\omega_r\right)\boldsymbol{\psi}^+_{sdq} \right. \\ &\quad \left. - \frac{j2(\omega_1 - \omega_r)\sigma L_s\boldsymbol{U}^+_{sdq}\boldsymbol{S}_s}{3U_s^2}\right\} \\ &\quad - \frac{\boldsymbol{U}^+_{sdq}}{U_s^2}\left\{\frac{2\left(L_r R_s + L_s R_r\right)}{3L_m} + \frac{2\sigma L_r L_s}{3L_m}\cdot\frac{d}{dt}\right\}\boldsymbol{S}_s \\ &= \boldsymbol{E}^+_{rdq} - \frac{\boldsymbol{U}^+_{sdq}}{U_s^2}\left\{\frac{2\left(L_r R_s + L_s R_r\right)}{3L_m} + \frac{2\sigma L_r L_s}{3L_m}\cdot\frac{d}{dt}\right\}\boldsymbol{S}_s \end{aligned} \tag{15}$$

where $\boldsymbol{E}^+_{rdq}$ is the decoupling voltage component.

Therefore, according to (15), the mathematical models of DFIG without PLL under distorted voltage conditions have been established, the DPC scheme of DFIG can be designed. The required rotor voltage can be obtained by regulating the stator active and reactive powers. Compared with the conventional DPC scheme, without the orientation of voltages or flux linkages, the coordinate frame may not be in accord with the actual voltage vector, so the both d and q axes voltage components need to be taken into account.

III. Proposed DPC Strategy Without PLL

Based on the mathematical models of DFIG without PLL, an improved DPC is proposed to improve the system performance under harmonically distorted voltage conditions. Since the stator active and reactive powers contain both average components and harmonic ones, the power controllers should be capable of regulating dc components and pulsating ones simultaneously.

Fig. 2 gives the schematic diagram of the proposed DPC strategy. In the control system, which is implemented in the synchronous reference frame rotating at $\omega_1 = 100\pi$ rad/s, the virtual angular $\theta_1 = \omega_1 t$ is used for coordinated transforma-

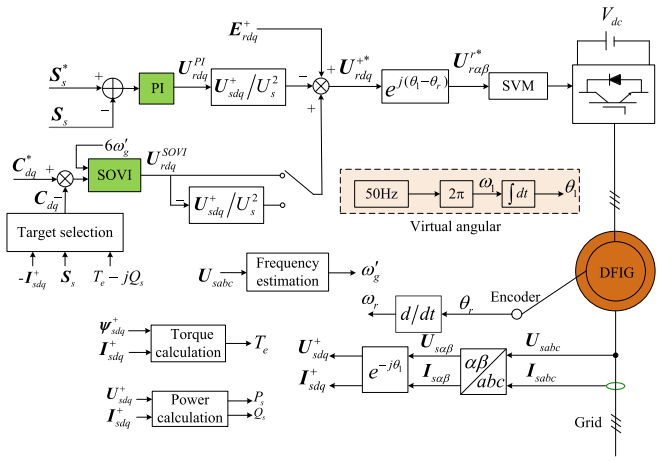

Fig. 2. Schematic diagram of the proposed DPC strategy.

tion. It has been indicated that the average active and reactive powers are dc signals regardless of the actual grid frequency deviation. Thus, PI controllers can be employed to eliminate the power errors so as to track the active and reactive power references even during frequency variation. As for pulsating components, an SOVI regulator is employed to implement direct resonant control to remove distorted currents and restrain power pulsations or electromagnetic torque ripples. Since the harmonic components of such electromagnetic quantities behave as fluctuations of $6\omega_g$ in this synchronous reference frame, the SOVI tuned at six times the grid frequency is introduced in the resonant closed-loop control.

Based on the pole-zero cancellation to eliminate the unexpected peak in the closed-loop control response [20], the SOVI can be expressed as

$$G_{SOVI}(s) = \frac{k_{pr}s^2 + k_{ir}s}{s^2 + 2\omega_c s + (6\omega'_g)^2} \tag{16}$$

where $\omega_c = 10\text{–}20\,rad/s$ is the cutoff frequency for increasing the resonant bandwidth, k_{pr} and $k_{ir} = k_{pr} \cdot Rr/\sigma Lr$ are the proportional and integral coefficients, respectively, ω'_g is the estimated grid frequency.

It should be highlighted that the SOVI in this paper is a frequency adaptive resonant controller, which guarantees the accurate harmonic suppression in the presence of frequency variation. The frequency estimation algorithm will be specifically discussed in Section IV.

According to the operation requirements of the DFIG system and the power quality standards under distorted voltage conditions, three alternative control targets of smooth stator active and reactive powers, sinusoidal stator current, and constant electromagnetic torque are investigated in this paper. It should be noted that the smooth electromagnetic torque will benefit the lifetime of mechanical components in the wind turbine. Though the rotor power also contains harmonic components, it should be noted that the power converter of DFIG consists of both rotor-side converter (RSC) and grid-side converter (GSC), and the dc-link capacitor can work as the buffer to suppress the power pulsation influence from the rotor side to the grid side. It should be also pointed out that the power pulsation in the rotor side is relatively smaller compared with the average power, and will not affect the safe operation of GSC. Thus, the rotor power pulsation was normally ignored in the research of the control strategy of the DFIG system [5], [8].

Since the SOVI can only provide infinite gain only at assigned ac signals and attenuate amplitude responses of other frequencies, electromagnetic quantities, including currents, powers, and electromagnetic torque, can be directly set as the controlled variables of the SOVI. Thus, the corresponding feedbacks of three different targets can be expressed as follows.

For *Target I,* to remove the pulsations of the stator active and reactive powers simultaneously, the feedback variable is obtained by

$$\boldsymbol{C}_{dq} = \boldsymbol{S}_S = P_s - jQ_s. \tag{17}$$

For *Target II*, to ensure sinusoidal stator current, the feedback variable is obtained by

$$\boldsymbol{C}_{dq} = -\boldsymbol{I}^+_{sdq} = -i^+_{sd} - ji^+_{sq}. \tag{18}$$

According to [21], the pulsations of DFIG reactive power and electromagnetic torque should be suppressed at the same time. Therefore, for *Target III*, to smooth the reactive power and electromagnetic torque, the feedback variable is obtained by

$$\boldsymbol{C}_{dq} = T_e - jQ_s. \tag{19}$$

Since the SOVI can only achieve a zero steady-state error at $6\omega'_g$, the commanded value of SOVI can be simply set as zero, i.e., $\boldsymbol{C}^*_{dq} = 0$.

Then, the commanded rotor voltage can be calculated by

$$\begin{cases} \boldsymbol{U}^{+*}_{rdq} = \boldsymbol{E}^+_{rdq} - \frac{\boldsymbol{U}^+_{sdq}}{U_s^2}\left(\boldsymbol{U}^{PI}_{rdq} + \boldsymbol{U}^{SOVI}_{rdq}\right), & Target\,I, III \\ \boldsymbol{U}^{+*}_{rdq} = \boldsymbol{E}^+_{rdq} - \frac{\boldsymbol{U}^+_{sdq}}{U_s^2} \cdot \boldsymbol{U}^{PI}_{rdq} + \boldsymbol{U}^{SOVI}_{rdq}, & Target\,II \end{cases}. \tag{20}$$

Thus, the commanded rotor voltage consists of three parts: $\boldsymbol{U}^{PI}_{rdq}$, $\boldsymbol{U}^{SOVI}_{rdq}$, and $\boldsymbol{E}^+_{rdq}$, which represent the average component produced by the PI controllers, the output of the SOVI and the decoupling voltage component, respectively.

Finally, the commanded rotor voltage is transformed to the stationary reference frame, and the space vector modulation (SVM) technique is employed to generate the required switching pulses.

It should be noted that the proposed DPC strategy eliminates the PLL and the relevant potential instability problems can be avoided. Meanwhile, the pulsations of electromagnetic quantities can be directly controlled through the direct-resonant scheme, so the sequential separations of the voltages and currents and the complex calculations of the power compensating items can also be eliminated. In this way, the simple system implementation and less computation burden can be achieved in the proposed DPC scheme.

IV. Adaptive Frequency Detection Algorithm

According to grid codes, the network always has the potential frequency variation, such as ± 1 Hz [16] and -3 Hz/$+2$ Hz [17].

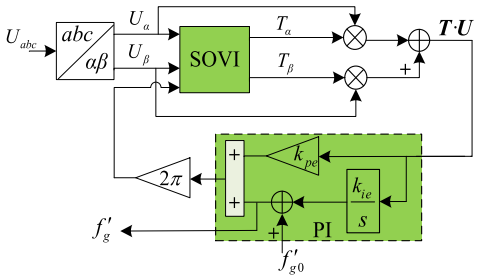

Fig. 3. Scheme diagram of the frequency estimation method.

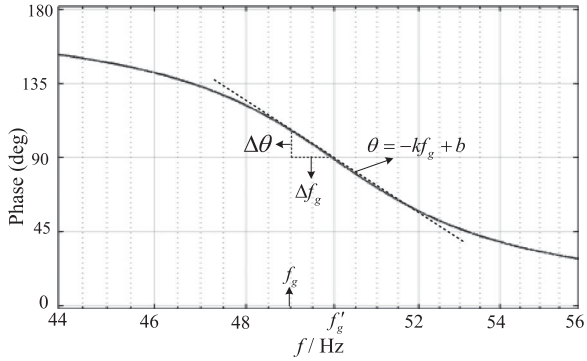

Fig. 4. Phase response of the SOVI with the resonant frequency of f_g' ($k_{pr} = 1, k_{ir} = 15.7, \omega_c = 20$ rad/s).

As indicated in [22], the control capability of resonant regulators on the harmonic frequency point will be weaken when the grid voltage frequency deviation occurs. In [5] and [23], the cutoff frequency is employed to deal with this problem, but it can only work within relatively narrow frequency deviation range. Another idea is to increase the amplitude gain of the resonant regulator by magnifying the proportional coefficient, whereas the system stability will be reduced due to the decreased phase margin [15].

In order to guarantee the harmonic suppression ability against frequency variation under distorted voltage conditions, an estimation algorithm of grid frequency is proposed. Thus, the resonant frequency of the SOVI in Fig. 2 is the instantaneous estimated result instead of fixed one, which provides the SOVI with real-time tracking ability in the harmonic frequency. Different from the estimation methods based on second order generalized integrator quadrature signal generator in a single-phase system [24], [25]; here, the phase characteristic of the resonant controller is directly employed to detect the actual frequency in three-phase systems. It should be noted that the frequency estimation algorithm in the following is also based on the SOVI.

Fig. 3 shows the scheme diagram of the frequency estimation method, which is based on an SOVI with the resonant frequency around 50 Hz. $\boldsymbol{U}$, a vector with actual grid frequency of f_g, is chosen as the input of the SOVI, while vector $\boldsymbol{T}$ is defined as the output, and θ is the phase difference between $\boldsymbol{U}$ and $\boldsymbol{T}$. f_g' represents the estimated frequency, which is also set as the resonant frequency of the SOVI. Since the grid frequency f_g is only allowed deviation around its nominal value, the initial value of f_g' can be set as $f_{g0}' = 50$ Hz. In order to demonstrate the frequency estimation mechanism, Fig. 4 shows the phase response of the SOVI with the resonant frequency of f_g'.

It can be seen in Fig. 4 that $f_g = f_g'$ and then $\theta = 90^\circ$ during steady state. When the grid frequency encounters a perturbation, for example, if $\theta > 90^\circ$, it means $f_g < f_g'$, and f_g' should decrease correspondingly. Besides, at the adjacent of f_g', θ and f_g behave as linear correlation, which can be written as

$$\theta = -kf_g + b \tag{21}$$

where k and b represent linear factor and constant, respectively, $k > 0$.

Therefore, the frequency estimation error can be expressed by $\Delta\theta$ as

$$\Delta f_g = -\frac{1}{k}\Delta\theta. \tag{22}$$

In this paper, $\Delta\theta$ can be derived from the dot product between $\boldsymbol{U}$ and $\boldsymbol{T}$ given by

$$\begin{aligned}\boldsymbol{T}\cdot\boldsymbol{U} &= |\boldsymbol{T}|\,|\boldsymbol{U}|\cos\theta \\ &= |\boldsymbol{T}|\,|\boldsymbol{U}|\cos(90^\circ + \Delta\theta) \approx -|\boldsymbol{T}|\,|\boldsymbol{U}|\,\Delta\theta.\end{aligned} \tag{23}$$

Once f_g' converges to f_g, $\boldsymbol{T}\cdot\boldsymbol{U}$ will decrease to zero. For simplicity, $\boldsymbol{T}\cdot\boldsymbol{U}$ can be directly chosen as the input error of the PI controller shown in Fig. 4, where the proportional is employed to accelerate the adjusting process to obtain fast convergence speed, and the integrator to remove the steady-state error. It should be highlighted that the integrator output, instead of the PI output, is set as the estimated frequency for a more smooth result and higher filtering capability [26]. Meanwhile, since the SOVI with resonant frequency around 50 Hz can attenuate amplitude responses at the harmonic frequencies, it functions as a filter for the harmonic input, which provides the frequency estimation algorithm with disturbance rejection capability under distorted voltage conditions.

It should be noted that the frequency estimation only serves for the frequency adaptive SOVI, which is not involved in power regulation loop and makes no difference to system stability. Meanwhile, compared with other estimation methods [27], [28], this method avoids the complex calculation of nonlinear trigonometric functions of park transformation, and provides the simple implementation and better dynamic response.

Thus, with the fast and accurate frequency estimation method, strong robustness against the grid frequency deviation can be achieved for the harmonic components suppression.

V. Control Performance Analysis

In order to validate the availability of the proposed DPC strategy for the DFIG under distorted voltage conditions, the disturbance rejection capability and dynamic response of the proposed strategy will be investigated in this section. Suppose that the grid frequency is 50 Hz, the SOVI for the suppression

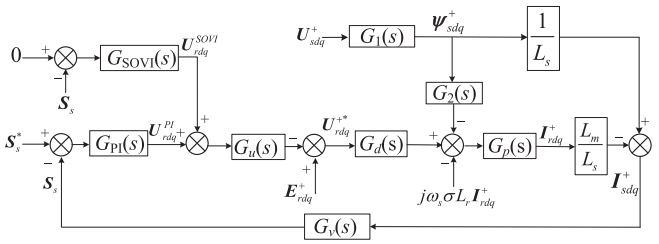

Fig. 5. Block diagram of the proposed scheme with *Target I*.

of the pulsating items is enabled with the resonant frequency of 300 Hz.

Based on (3) and (4), the stator flux linkage can be expressed as

$$\boldsymbol{\psi}_{sdq}^{+} = \frac{1}{s+j\omega_1}\boldsymbol{U}_{sdq}^{+} - \frac{R_s}{s+j\omega_1}\boldsymbol{I}_{sdq}^{+} \tag{24}$$

$$\boldsymbol{I}_{sdq}^{+} = \frac{1}{L_s}\boldsymbol{\psi}_{sdq}^{+} - \frac{L_m}{L_s}\boldsymbol{I}_{rdq}^{+}. \tag{25}$$

If the stator resistance R_s is neglected, (24) can be simplified as

$$\boldsymbol{\psi}_{sdq}^{+} = \frac{1}{s+j\omega_1}\boldsymbol{U}_{sdq}^{+}. \tag{26}$$

According to (3) and (4), the rotor voltage can be expressed as

$$\begin{aligned}\boldsymbol{U}_{rdq}^{+} = {} & (R_r+\sigma L_r s)\boldsymbol{I}_{rdq}^{+} + j\omega_s\sigma L_r\boldsymbol{I}_{rdq}^{+} \\ & + \frac{L_m}{L_s}(s+j\omega_s)\boldsymbol{\psi}_{sdq}^{+}.\end{aligned} \tag{27}$$

Thus, based on (5), (18), (20), (25)–(27), the block diagram of the proposed control strategy is shown in Fig. 5, in which *Target I* of removing the pulsations of the stator active and reactive powers is selected to implement the performance analysis. $G_p(s)$ describes the mathematic model of the DFIG. $G_d(s)$ represents the computation delay. Then, $G_1(s)$, $G_2(s)$, $G_p(s)$, $G_u(s)$, $G_v(s)$, and $G_d(s)$ can be described by

$$G_1(s) = \frac{1}{s+j\omega_1} \tag{28}$$

$$G_2(s) = \frac{L_m}{L_s}(s+j\omega_s) \tag{29}$$

$$G_u(s) = \frac{\boldsymbol{U}_{sdq}^{+}}{U_s^2} \tag{30}$$

$$G_v(s) = 1.5\hat{\boldsymbol{U}}_{sdq}^{+} \tag{31}$$

$$G_p(s) = \frac{1}{R_r+\sigma L_r s} \tag{32}$$

$$G_d(s) = \frac{1}{1+sT_d} \tag{33}$$

where T_d is the delay time.

Therefore, the transfer functions $F_{us}(s)$ and $F_{ss}(s)$ can be deduced as

$$\frac{\boldsymbol{S}_s}{\boldsymbol{U}_{sdq}^{+}} = F_{us}(s) \tag{34}$$

$$\frac{\boldsymbol{S}_s}{\boldsymbol{S}_s^{*}} = F_{ss}(s) \tag{35}$$

where $F_{us}(s)$ is the transfer function from the grid voltage $\boldsymbol{U}_{sdq}^{+}$ to powers $\boldsymbol{S}_s$, which represents the rejection capability to voltage disturbances of the proposed strategy, $F_{ss}(s)$ is the transfer function from the active and reactive power reference $\boldsymbol{S}_s^{*}$ to $\boldsymbol{S}_s$, which represents the dynamic response of the proposed strategy. The corresponding transfer functions can be expressed as

$$F_{us}(s) = \frac{G_1(s)G_v(s)/L_s + G_1(s)G_2(s)G_p(s)G_v(s)L_m/L_s}{1+1.5\left[G_{PI}(s)+G_{SOVI}(s)\right]G_p(s)G_d(s)L_m/L_s} \tag{36}$$

$$F_{ss}(s) = \frac{G_{PI}(s)G_u(s)G_v(s)G_p(s)G_d(s)L_m/L_s}{1+1.5\left[G_{PI}(s)+G_{SOVI}(s)\right]G_p(s)G_d(s)L_m/L_s}. \tag{37}$$

However, $G_v(s)$ in (36) also represents voltage components, so $F_{us}(s)$ cannot directly evaluate the rejection capability to voltage disturbances of the proposed strategy. According to (36), a new transfer function F_{u2s}(s), from the square of voltage amplitude U_s^2 to powers $\boldsymbol{S}_s$, can be deduced as

$$\begin{aligned}F_{u2s}(s) &= \frac{\boldsymbol{S}_s}{U_s^2} \\ &= \frac{1.5G_1(s)/L_s + 1.5G_1(s)G_2(s)G_p(s)L_m/L_s}{1+1.5\left[G_{PI}(s)+G_{SOVI}(s)\right]G_p(s)G_d(s)L_m/L_s}.\end{aligned} \tag{38}$$

It should be noted that though the stator voltage amplitude U_s can be appropriately regarded as constant for simplified analysis during the mathematical modeling of DFIG, in the actual control system, U_s is measured instantaneously by voltage sensors. Under distorted voltage conditions, the stator voltage contains fundamental components of dc signals, and the harmonic ones of $6\omega_g$, supposed that ω_g is equal to ω_1. In the virtual $(dq)^+$ synchronous reference frame, U_s^2 can be expressed as

$$U_s^2 = u_{sd}^{+2} + u_{sq}^{+2} = \left(u_{sd0}^{+} + u_{sd6}^{+}\right)^2 + \left(u_{sq0}^{+} + u_{sq6}^{+}\right)^2 \tag{39}$$

where u_{sd0}^{+} and u_{sq0}^{+} represent the fundamental voltage components of *d* and *q* axes voltage, u_{sd6}^{+} and u_{sq6}^{+} represent the harmonic ones of *d* and *q* axes voltage, respectively.

Then, (39) can be calculated as

$$\begin{aligned}U_s^2 &= u_{sd0}^{+2} + u_{sq0}^{+2} + 2u_{sd0}^{+}u_{sd6}^{+} + 2u_{sq0}^{+}u_{sq6}^{+} + u_{sd6}^{+2} + u_{sq6}^{+2} \\ &\approx u_{sd0}^{+2} + u_{sq0}^{+2} + 2u_{sd0}^{+}u_{sd6}^{+} + 2u_{sq0}^{+}u_{sq6}^{+}\end{aligned} \tag{40}$$

where $u_{sd6}^{+2} + u_{sq6}^{+2}$ is neglected. Since the proportion of harmonic voltage components is relatively smaller compared with the fundamental ones, the corresponding square values can be neglected.

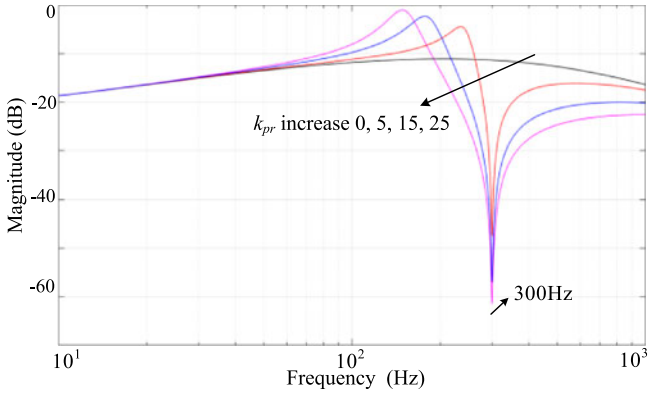

Fig. 6. Magnitude response of $F_{u2s}(s)$ ($k_{pr} = 0, 5, 15, 25$, $\omega_c = 15$ rad/s, $R_r = 0.88\,\Omega$, $L_s = L_r = 0.093$ H, $L_m = 0.09$ H).

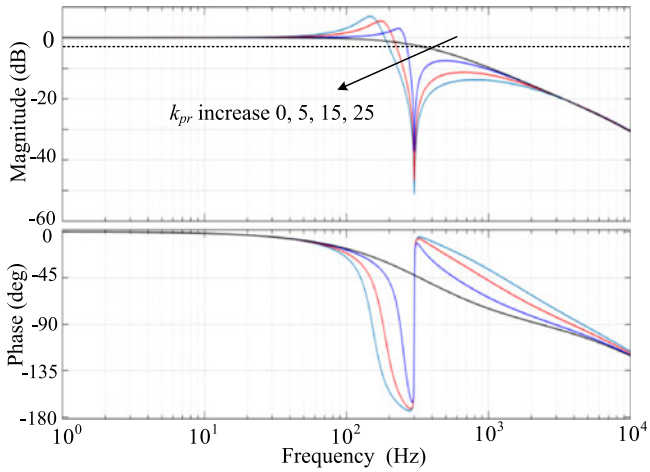

Fig. 7. Bode diagram of $F_{ss}(s)$ ($k_{pr} = 0, 5, 15, 25, \omega_c = 15$ rad/s, $R_r = 0.88\,\Omega$, $L_s = L_r = 0.093$ H, $L_m = 0.09$ H).

Thus, according to (40), U_s^2 can also represent the fundamental components and harmonic ones of the stator voltage, which act as voltage disturbances to the powers $\boldsymbol{S}_s$. Therefore, $F_{u2s}(s)$ actually represents the rejection capability to voltage disturbances of the proposed control strategy.

Fig. 6 gives the magnitude response of $F_{u2s}(s)$, where $k_{pr} = 0$ represents the SOVI is disabled. The magnitude response at 300 Hz is -11.2 dB when only PI controller is employed with $k_{pr} = 0$. The relevant magnitude responses decrease to -47.5 and -57.1, and -61.4 dB when $k_{pr} = 5$, 15, and 25, respectively. It should be noted that the lower magnitude responses at $6\omega_g$ mean the greater antidisturbance ability. Thus, the proposed control scheme can significantly decrease the magnitude responses at 300 Hz so as to enhance the rejection capability to harmonic voltages for the DFIG system.

It is also important to investigate the dynamic responses of active and reactive powers for the proposed control strategy. The bode diagram of $F_{ss}(s)$ is shown in Fig. 7. Note that if $k_{pr} = 0$, it is identically to use a PI controller with the SOVI disabled. It can be seen that the cutoff frequency, i.e., the minimum frequency for -3-dB attenuation, is 345, 267, 225, and 198 Hz when $k_{pr} = 0$, 5, 15, and 25, respectively. Thus, the introduced

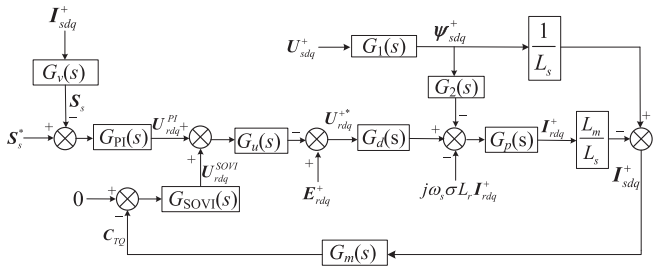

Fig. 8. Block diagram of the proposed scheme with *Target III*.

SOVI results in the fact that the cutoff frequency decreases while k_{pr} increases, which might degrade the dynamic responses with the step change of stator active and reactive powers [29]. It can be concluded that proportional coefficient $k_{\rm pr}$ should be carefully selected with the tradeoff between the rejection capability of voltage disturbances and dynamic response of the DFIG system.

Since the performance analysis process of *Target II* is similar to the one of *Target I,* the block diagram and performance analysis of the proposed control strategy with *Target II* will not be illustrated in this section. As for *Target III* of the smooth reactive power and electromagnetic torque, the corresponding disturbance rejection capability of the proposed strategy will be investigated as follows.

According to (6), the electromagnetic torque can be also expressed as

$$T_e = -1.5 n_p \mathrm{Re}\left\{\hat{\boldsymbol{\psi}}^+_{sdq} \cdot j\boldsymbol{I}^+_{sdq}\right\} \tag{41}$$

where Re represents the real part.

Since the differential of stator flux linkage $\boldsymbol{\psi}^+_{sdq}$ can be regard as 0 regardless of the dynamic transient, (26) can be rewritten as

$$\boldsymbol{U}^+_{sdq} = j\omega_1 \boldsymbol{\psi}^+_{sdq}. \tag{42}$$

Then, according to (41) and (42), the reactive power can be expressed as

$$Q_s = \omega_1 Im\left\{\hat{\boldsymbol{\psi}}^+_{sdq} \cdot j\boldsymbol{I}^+_{sdq}\right\}. \tag{43}$$

Thus, the following relation can be obtained

$$\boldsymbol{C}_{TQ} = T_e + j\frac{m}{\omega_1} Q_s = m\hat{\boldsymbol{\psi}}^+_{sdq} \cdot j\boldsymbol{I}^+_{sdq} \tag{44}$$

where $m = -1.5 n_p$, $\boldsymbol{C}_{TQ}$ is a vector consisting of T_e and Q_s.

Thus, $\boldsymbol{C}_{TQ}$ can be employed to represent the feedback variable of *Target III*, i.e., $\boldsymbol{C}_{dq} = T_e - jQ_s$. Then, the block diagram of the proposed control strategy with *Target III* is shown in Fig. 8.

To evaluate the disturbance rejection capability of the proposed strategy, the transfer function $F_{ut}(s)$ from the voltage disturbance $\boldsymbol{U}^+_{sdq}$ to $\boldsymbol{C}_{TQ}$ should be derived. According to Fig. 8,

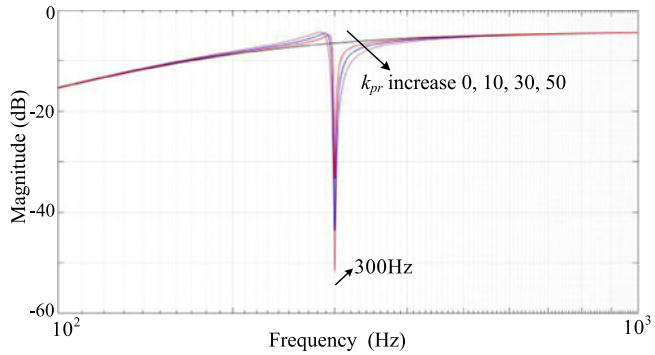

Fig. 9. Magnitude response of $F_{u2t}(s)$ ($k_{pr} = 0, 10, 30, 50$, $\omega_c = 15$ rad/s, $R_r = 0.88\,\Omega$, $L_s = L_r = 0.093$ H, $L_m = 0.09$ H).

$F_{ut}(s)$ can be deduced as

$$F_{ut}(s) = \frac{\boldsymbol{C}_{TQ}}{\boldsymbol{U}^+_{sdq}} = \frac{G_1(s)G_m(s)/L_s + G_1(s)G_2(s)G_p(s)G_m(s)L_m/L_s}{1 + [1.5G_{PI}(s) + G_3(s)G_{SOVI}(s)]\,G_p(s)G_d(s)L_m/L_s} \tag{45}$$

where $G_m(s) = jm\hat{\psi}^+_{sdq} = jm\hat{G}_1(s)\hat{\boldsymbol{U}}^+_{sdq} = G_3(s)\hat{\boldsymbol{U}}^+_{sdq}$.

Similar to the problem indicated for $F_{us}(s)$, $G_m(s)$ in (45) contains voltage components, so $F_{ut}(s)$ cannot directly evaluate the rejection capability to voltage disturbances of the proposed strategy. According to (45), a transfer function $F_{u2t}(s)$, from the square of voltage amplitude U_s^2 to $\boldsymbol{C}_{TQ}$, can be obtained as

$$F_{u2t}(s) = \frac{\boldsymbol{C}_{TQ}}{U_s^2} = \frac{G_1(s)G_3(s)/L_s + G_1(s)G_2(s)G_3(s)G_p(s)L_m/L_s}{1 + [1.5G_{PI}(s) + G_3(s)G_{SOVI}(s)]\,G_p(s)G_d(s)L_m/L_s}. \tag{46}$$

According to (40), $F_{u2t}(s)$ actually represents the rejection capability to voltage disturbances of the proposed control strategy with *Target III*.

Fig. 9 gives the magnitude response of $F_{u2t}(s)$. The magnitude response at 300 Hz is -7.5 dB when $k_{pr} = 0$ with the PI controller employed. The relevant magnitude responses decrease to -33.6 and -43.2 dB and -51.8 dB when $k_{pr} = 10$, 30, and 50, respectively. It can be concluded that with the proposed control scheme, the magnitude response at 300 Hz can be reduced significantly, so the rejection capability to harmonic voltages can be validated and *Target III* of smooth reactive power and electromagnetic torque can be achieved.

VI. Experimental Results

In order to validate the effectiveness of the proposed control scheme, experimental tests were carried out on laboratory prototype of a 1-kW DFIG system. In this system, the DFIG is driven by a 1.5-kW squirrel cage induction machine as the wind turbine. A Chroma programmable ac source 61704 is used to simulate the network, including practical harmonic power grid and grid frequency variation. The control strategy is implemented on a TI TMS320F28335 DSP. The RSC of DFIG is connected with a dc power supply. In order to simplify the paper contents and highlight the DFIG control performance with the proposed strategy, the control of GSC is neglected in this test as [8]. The rotor speed is initially set to 800 r/min, where the synchronous speed is 1000 r/min. All waveforms are acquired by a YOKOGAWA DL750 scope recorder. And the parameters of the tested DFIG system are listed in Table I. During the experiment, the fifth-and seventh-harmonic components of the grid voltage are set to be 5.73% and 4.77%, respectively.

TABLE I
Parameters of the Experimental DFIG System

Rate power	1 kW	$L_{\sigma s}$	3.0 mH
Stator voltage	120 V	Stator/rotor turns ratio	0.33
L_m	90.1 mH	Popar Paris	3
R_s	1.01 Ω	DC bus voltage	280 V
$L_{\sigma s}$	3.0 mH	Switching frequency	10 kHz
R_r	0.88 Ω	Sampling frequency	10 kHz

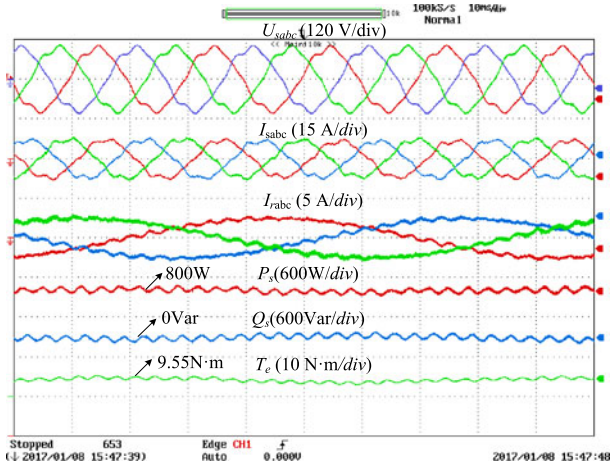

Fig. 10. Experimental results under distorted voltage conditions (10 ms/div).

Fig. 10 shows the experimental results under distorted voltage conditions when the SOVI is disabled. The network frequency is initially set at 50 Hz, and the active and reactive powers are set at 800 W and 0 Var, respectively. The stator current contains 8.11% 250 Hz and 4.74% 350 Hz harmonic components due to the influence of the harmonic voltage components. Besides, the stator active and reactive power pulsations would increase to ±41.8 W and ±44.1 Var. And the generator torque ripples account for nearly 5.40%.

In order to effectively restrain pulsations caused by distorted voltage components, especially in the case of the frequency deviation, the grid frequency estimation algorithm should be first verified. Fig. 11 shows the experimental results during a frequency deviation from 50 to 48 Hz under distorted voltage conditions. It should be noted that caused by the undesired natural flux linkages, the low-frequency oscillations appear in the powers during a transient frequency variation, which can be solved by a demagnetizing current control scheme [18]. In this case, *Target I* is enabled using a

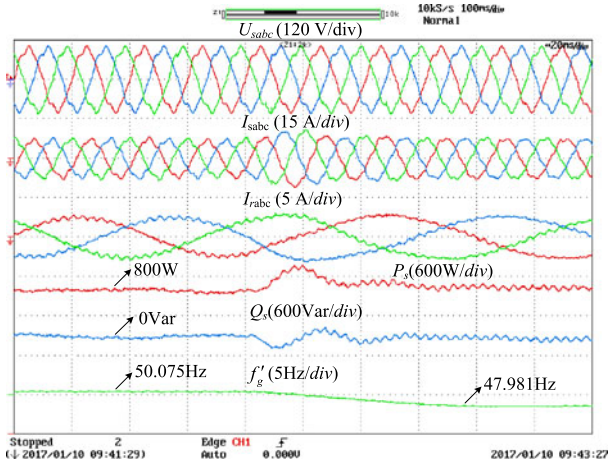

Fig. 11. Experimental results during a frequency deviation from 50 to 48 Hz with *Target I* using a conventional SOVI (20 ms/div).

conventional SOVI with the resonant frequency of 300 Hz, which is effective when the grid frequency is 50 Hz. And the stator active and reactive power pulsations are suppressed to ± 8.8 W and ± 9.1 Var. However, when the grid frequency step changes to 48 Hz, the pulsations can no longer be significantly restrained since the harmonic suppression ability is weaken with the deviation of the harmonic components frequency. Fig. 11 also shows the estimated frequency by the estimation algorithm. When the grid frequency f_g varies instantly, the estimated frequency f'_g converges to the actual one with a transient time of 0.07 s, from 50.075 to 47.981 Hz, where the estimation error is within 0.15%. Thus, the fast and accurate frequency detection can be achieved, which will be employed in the frequency adaptive SOVI.

With the accurate frequency detection, the harmonic components can be precisely suppressed and all the alternative control targets can be achieved with frequency adaptive SOVI during 48 Hz grid frequency shown in Fig. 12(a)–Fig. 12(c). As for *Target I*, the 288 Hz pulsations of the active and reactive powers are reduced to ± 7.8 W and ± 8.2 Var, respectively. When *Target II* is enabled, sinusoidal stator current is achieved, with fifth- and seventh-harmonic components accounting for 0.91% and 0.31%, respectively. As for *Target III*, the torque ripples can be restrained to 1.5%, while the pulsations of the reactive power decrease to ± 8.1 Var.

In order to further evaluate the validity of the proposed control scheme, the dynamic response tests are carried out in Fig. 13. Fig. 13(a) shows the result of *Target I* with the frequency adaptive SOVI during a frequency variation from 49 to 51 Hz. After the frequency deviates, the active and reactive powers remain smooth within 0.07 s, with the estimated frequency from 49.015 to 51.01 Hz. In Fig. 13(b), when the operation mode switches among *Target I–III*, relevent control targets can be achieved rapidly. Fig. 13(c) shows the dynamic power tracking ability when the stator active and reactive powers stepped from 500 to 800 W and 0 to 300 Var, respectively. It can be seen that the DFIG power tracking takes a short response time of around 10 ms. Meanwhile, with *Target II* active, the stator current maintains

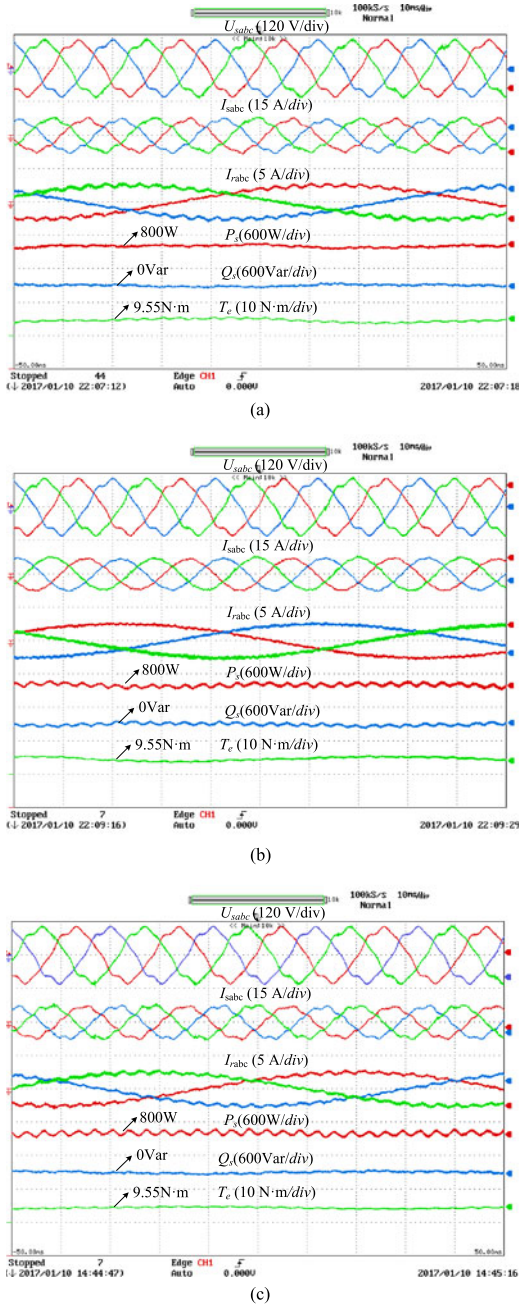

Fig. 12. Experimental results of the proposed control scheme with frequency adaptive SOVI during 48 Hz grid frequency (10 ms/div). (a) *Target I*. (b) *Target II*. (c) *Target III*.

sinusoidal both before and after the stepping moment. Thus, the proposed control scheme can provide fast tracking and satisfactory independent regulations of the active and reactive powers. Fig. 13(d) shows the DFIG performance with rotor speed from 800 (subsynchronous) to 1200 r/min (supersynchronous) during 48 Hz grid frequency. In this process, *Target I* is ensured with smooth active and reactive powers, and the rotor current changes with no overcurrent. Therefore, the proposed control scheme can guarantee excellent dynamic response performance under distorted voltage conditions.

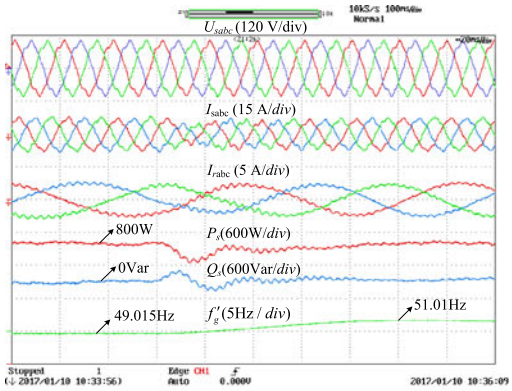

(a)

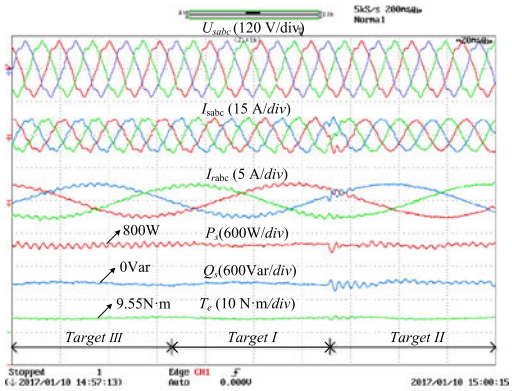

(b)

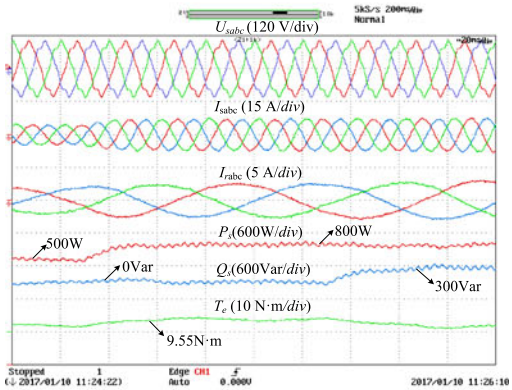

(c)

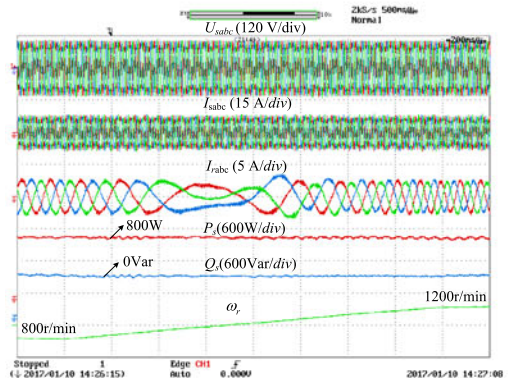

(d)

Fig. 13. Dynamic responses of the proposed control scheme. (a) *Target I* is selected during a frequency deviation from 49 to 51 Hz (20 ms/div). (b) Different control targets switch (20 ms/div). (c) Active and reactive powers step change with *Target II* (20 ms/div). (d) DFIG speeds up from 800 to 1200 r/min with

VII. Conclusion

This paper proposes an improved DPC strategy for the DFIG without PLL under distorted voltage conditions, in which a frequency adaptive harmonic suppression scheme based on the frequency estimation algorithm is employed. For a clear statement, the following conclusions can be highlighted.

1) The proposed DPC strategy is implemented in a synchronous reference frame rotating at fixed angular speed. Thus, the PLL can be avoided and its potential instability problems can be eliminated.
2) The SOVI is integrated with DPC to directly eliminate the harmonic components of currents, powers, or electromagnetic torque alternatively. Thus, sequential separations of the voltages and currents and complex calculations of power compensations can be removed, which provides a simple implementation and less computation burden.
3) In order to guarantee the harmonic suppression ability against grid frequency variation, a frequency estimation algorithm is proposed, and it has been proved that the frequency adaptive SOVI can precisely eliminate harmonic distortions with real-time tracking ability.

References

[1] S. Muller, M. Deicke, and R. W. De Doncker, "Doubly fed induction generator systems for wind turbines," *IEEE Ind. Appl. Mag.*, vol. 8, no. 3, pp. 26–33, May/Jun. 2002.
[2] F. Blaabjerg, M. Liserre, and K. Ma, "Power electronics converters for wind turbine systems," *IEEE Trans. Ind. App.*, vol. 48, no. 2, pp. 708–719, Mar./Apr. 2012.
[3] M. Malinowski, M. Jasinski, and M. P. Kazmierkowski, "Simple direct power control of three-phase PWM rectifier using space-vector modulation (DPC-SVM)," *IEEE Trans. Ind. Electron.*, vol. 51, no. 2, pp. 447–454, Apr. 2004.
[4] G. K. Singh, "Power system harmonics research: A survey," *Euro. Trans Elect. Power*, vol. 19, no. 2, pp. 151–172, Aug. 2007.
[5] J. B. Hu, H. L. Xu, and Y. K. He, "Coordinated control of DFIG's RSC and GSC under generalized unbalanced and distorted grid voltage conditions," *IEEE Trans. Ind. Electron.*, vol. 60, no. 7, pp. 2808–2819, Jul. 2013.
[6] H. L. Xu, J. B. Hu, and Y. K. He, "Integrated modeling and enhanced control of DFIG under unbalanced and distorted grid voltage conditions," *IEEE Trans. Energy Convers.*, vol. 27, no. 3, pp. 725–736, Jun. 2012.
[7] J. Eloy-Garcia, S. Arnaltes, and J. L. Rodriguez-Amenedo, "Direct power control of voltage source inverters with unbalanced grid voltages," *IET Power Electron.*, vol. 1, no. 3, pp. 395–407, Sep. 2008.
[8] H. Nian and Y. P. Song, "Direct power control of doubly fed induction generator under distorted grid voltage," *IEEE Trans. Power Electron.*, vol. 29, no. 2, pp. 894–905, Feb. 2014.
[9] P. Rodriguez, A. Luna, I. Candela, R. Mujal, R. Teodorescu, and F. Blaabjerg, "Multiresonant frequency-locked loop for grid synchronization of power converters under distorted grid conditions," *IEEE Trans. Ind. Electron.*, vol. 58, no. 1, pp. 127–138, Jan. 2011.
[10] X. Q. Guo, W. Y. Wu, and Z. Chen, "Multiple-complex coefficient-filter based phase-locked loop and synchronization technique for three-phase grid-interfaced converters in distributed utility networks," *IEEE Trans. Ind. Electron.*, vol. 58, no. 4, pp. 1194–1204, Apr. 2011.
[11] B. Wen, D. Boroyevich, R. Burgos, P. Mattavelli, and Z. Y. Shen, "Analysis of d-q small-signal impedance of grid-tied inverters," *IEEE Trans. Power Electron.*, vol. 31, no. 1, pp. 675–687, Jan. 2016.
[12] M. Cespedes and J. Sun, "Impedance modeling and analysis of grid-connected voltage-source converters," *IEEE Trans. Power Electron.*, vol. 29, no. 3, pp. 1254–1261, Mar. 2014.
[13] D. Dong, B. Wen, D. Boroyevich, P. Mattavelli, and Y. S. Xue, "Analysis of phase-locked loop low-frequency stability in three-phase grid-connected power converters considering impedance interactions," *IEEE Trans. Ind. Electron.*, vol. 62, no. 1, pp. 310–321, Jan. 2015.

[14] P. Cheng and H. Nian, "Direct power control of voltage source inverter in a virtual synchronous reference frame during frequency variation and network unbalance," *IET Power Electron.*, vol. 9, no. 3, pp. 502–511, Mar. 2016.
[15] H. Nian, P. Cheng, and Z. Q. Zhu, "Coordinated direct power control of DFIG system without phase-locked loop under unbalanced grid voltage conditions," *IEEE Trans. Power Electron.*, vol. 31, no. 4, pp. 2905–2918, Jul. 2016.
[16] *Compatibility Levels for Low-Frequency Conducted Disturbances and Signaling in Public Low-Voltage Power Supply System*, IEC Standard 61000-2-2, 2002.
[17] *Voltage Characteristics of Electricity Supplied by Public Distribution Networks*, EN Standard 50160, 2011.
[18] H. Nian, P. Cheng, and Z. Q. Zhu, "Direct power control of doubly fed induction generator without phase-locked loop in synchronous reference frame during frequency variations," *IET Renewable Power Gener.*, vol. 9, no. 6, pp. 576–586, Aug. 2015.
[19] "Planning levels for harmonic voltage distortion and the connection of non-linear loads to transmission systems and distribution network in the United Kingdom," Electricity Association Engineering Recommendation G5/4-1, 2005.
[20] C. Lascu, L. Asiminoaei, I. Boldea, and F. Blaabjerg, "Frequency response analysis of current controllers for selective harmonic compensation in active power filters," *IEEE Trans. Ind. Electron.*, vol. 56, no. 2, pp. 337–347, Feb. 2009.
[21] J. B. Hu, H. Nian, and H. L. Xu, "Dynamic modeling and improved control of DFIG under distorted grid voltage conditions," *IEEE Trans. Energy Convers.*, vol. 26, no. 1, pp. 163–175, Oct. 2011.
[22] S. G. Jorge, C. A. Busada, and J. A. Solsona, "Frequency-adaptive current controller for three-phase grid-connected converters," *IEEE Trans. Ind. Electron.*, vol. 60, no. 10, pp. 4169–4177, Jul. 2013.
[23] Y. P. Song and H. Nian, "Modularized control strategy and performance analysis of DFIG system under unbalanced and harmonic grid voltage," *IEEE Trans. Power Electron.*, vol. 30, no. 9, pp. 4831–4842, Oct. 2015.
[24] P. Rodriguez, A. Luna, I. Etxeberria, J. R. Hermoso, and R. Teodorescu, "Multiple second order generalized integrators for harmonic synchronization of power converters," in *Proc. IEEE Energy Convers. Congr. Expo.*, 2009, pp. 2239–2246.
[25] T. Ngo, Q. Nguyen, and S. Santoso, "Improving performance of single-phase SOGI-FLL under DC-offset voltage condition," in *Proc. 40th Annu. Conf. IEEE Ind. Electron. Soc.*, 2014, pp. 1537–1541.
[26] S. Golestan, J. M. Guerrero, and J. C. Vasquez, "Three-phase PLLs: A review of recent advances," *IEEE Trans. Power Electron.*, vol. 32, no. 3, pp. 1894–1907, May 2017.
[27] M. S. Padua, S. M. Deckmann, and F. P. Marafao, "Frequency-adjustable positive sequence detector for power conditioning applications," in *Proc. IEEE Power Electron. Spec. Conf.*, 2005, pp. 1928–1934.
[28] F. D. Freijedo, A. G. Yepes, Ó. López, A. Vidal, and J. D. Gandoy, "Three-phase PLLs with fast postfault retracking and steady-state rejection of voltage unbalance and harmonics by means of lead compensation," *IEEE Trans. Power Electron.*, vol. 26, no. 1, pp. 85–97, Jun. 2011.
[29] V.-T. Phan and H.-H. Lee, "Performance enhancement of stand-alone DFIG systems with control of rotor and load side converters using resonant controllers," *IEEE Trans. Ind. Electron.*, vol. 48, no. 1, pp. 199–210, Jan. 2012.

Heng Nian (M'09–SM'14) received the B.Eng. and M.Eng. degrees from HeFei University of Technology, Hefei, China, and the Ph.D. degree from Zhejiang University, Hangzhou, China, in 1999, 2002, and 2005, respectively, all in electrical engineering.

From 2005 to 2007, he was a Postdoctoral in the College of Electrical Engineering, Zhejiang University. In 2007, he was promoted as an Associate Professor. From 2013 to 2014, he was a visiting scholar in the Department of Electrical, Computer, and System Engineering, Rensselaer Polytechnic Institute, Troy, NY. Since 2016, he has been a Full Professor at the College of Electrical Engineering, Zhejiang University. He has published more than 20 IEEE/IET transaction papers and holds more than 20 issued/pending patents. His current research interests include the optimal design and operation control for wind power generation system.

Longqi Li was born in Maoming, China. He received the B.Eng. degree in 2015 and works towards the M.Eng. degree at present in Zhejiang University, Hangzhou, China, all in electrical engineering.

His research interests include wind power generation system and doubly fed induction generator control.